

# Aqueous-Oxygen Corrosion Damage of 2.5D Braided SiC<sub>f</sub>/SiC Composites Prepared by CVI+PIP Processing: Multidimensional Observation and Mechanism Analysis

Zhang Lin<sup>\*1, 2</sup>, Li Junsheng<sup>\*2</sup>, Chen Sian<sup>\*2</sup>, Zhang Yanhu<sup>\*1</sup>, Wan Fan<sup>\*2</sup>

<sup>1</sup>School of Mechanical Engineering, Jiangsu University, No. 301 Xuefu Road, Zhenjiang 212013, China

<sup>2</sup>Science and Technology on Advanced Ceramic Fibers and Composites Laboratory, College of Aerospace Science and Engineering, National University of Defense Technology, Changsha 410073, China

received March 10, 2025; received in revised form March 27, 2025; accepted April 15, 2025

## Abstract

X-ray computed tomography (XCT) was utilized to perform quantitative and qualitative characterizations of aqueous-oxygen corrosion evolution in SiC<sub>f</sub>/SiC composites under pre- and post-oxidation conditions. The results indicate that the SiC matrix formed with the precursor impregnation and pyrolysis (PIP) method is located mainly in the inter-bundle region, which experiences significant oxidation after 160 hours of oxidation. This oxidation results in the formation of SiO<sub>2</sub> that fills the inter-bundle pores, leading to a decrease in porosity from an initial 10.9 % to 6.8 %. The interconnected inter-bundle pore network facilitates the ingress of oxygen, resulting in corrosion damage that is initiated preferentially at pore periphery regions. Progressive aqueous-oxygen corrosion leads to pore channel narrowing with surface smoothing, accompanied by the formation of vesicular porosity along the specimen periphery. A connected sheet-like and layered oxide skeleton structure forms finally because of the corrosion of matrix in the inter-bundle region.

*Keywords:* X-ray computed tomography (XCT), SiC<sub>f</sub>/SiC composites, high-temperature aqueous-oxygen, oxidation mechanism.

## I. Introduction

SiC<sub>f</sub>/SiC composite materials exhibit excellent properties, including high specific strength, high specific modulus, good high-temperature stability and wear resistance, outstanding radiation resistance, and low induced radioactivity. These advantages make them an ideal material choice for various fields, including nuclear energy<sup>1,2</sup>, aerospace<sup>3,4</sup>, and advanced energy systems<sup>5,6</sup>. Particularly in the aerospace sector, SiC<sub>f</sub>/SiC is considered an ideal material for manufacturing high-temperature components, such as structural parts for jet engines<sup>7,8</sup> and thermal protection systems (TPS)<sup>9,10,11</sup>.

As SiC<sub>f</sub>/SiC composite materials are used in high-temperature environments, their oxidative resistance is one of the critical properties that must be studied. In recent years, scholars have extensively researched the high-temperature oxidation behavior of SiC<sub>f</sub>/SiC composites. For instance, Wang *et al.*<sup>12</sup> performed oxidation experiments on SiC<sub>f</sub>/SiC composites at different temperatures and durations, analyzing mass changes and oxidation rates to explore their oxidation mechanisms. Luo *et al.*<sup>13</sup> simulated high-temperature oxidation of SiC<sub>f</sub>/SiC composites in air at 500–1100 °C, assessing the preservation of material properties before and after oxidation. With the deepening study of SiC<sub>f</sub>/SiC composites, particularly concerning

the actual working conditions encountered in aerospace engine combustion chambers where high-temperature aqueous vapor is prevalent, resistance to aqueous-oxygen corrosion has become a new focal point in researching the oxidative performance of SiC<sub>f</sub>/SiC composites. For example, Ji *et al.*<sup>14</sup> investigated the oxidation behavior of SiC<sub>f</sub>/SiC-SiBCN composites in H<sub>2</sub>O/O<sub>2</sub> and H<sub>2</sub>O/O<sub>2</sub>/Na<sub>2</sub>SO<sub>4</sub> environments, finding that the oxidation rate constant significantly increases with temperature. Notably, at 1350 °C, they observed the formation of a loose-layered oxide, which accelerated the oxidation of the material. Li *et al.*<sup>15</sup> prepared SiC/SiC-SiYC composites by means of CVI and reactive melt infiltration (RMI) processes, studying their corrosion behavior in an aqueous-oxygen environment. They found that the oxide layer formed during oxidation effectively protected the material, allowing it to maintain high flexural strength even at 1300 °C. However, existing studies primarily rely on superficial analyses based on weight changes or surface observations using two-dimensional characterization techniques such as scanning electron microscopy (SEM). These analytical methods either damage the samples or lack comprehensiveness, resulting in an insufficiently thorough understanding of the aqueous-oxygen oxidation processes and mechanisms affecting SiC<sub>f</sub>/SiC composites.

\* Corresponding author: wanfan12@nudt.edu.cn

In recent years, there has been increasing research on the application of XCT technology for non-destructive testing of material structures. This technology can provide detailed information about the internal microstructure of materials, including the location and morphology of pores, cracks, and other defects, without damaging the samples. Wang *et al.*<sup>16</sup> utilized XCT technology to perform 3D characterization of porosity and damage in C/SiC composites, revealing the relationship between porosity and damage mechanisms. Puchakayla *et al.*<sup>17</sup> investigated defect evolution during the manufacturing of yttria-stabilized zirconia ceramics using digital light processing (DLP) sintering through XCT, exploring changes in porosity and surface roughness from both two-dimensional and 3D perspectives, as well as the effects of peak sintering temperature on density, grain growth, and surface roughness. Niu *et al.*<sup>18</sup> visualized the 3D geometric morphology of C/SiC composites under tensile testing using XCT and revealed the evolution process of internal damage. Lo *et al.*<sup>19</sup> characterized the microstructure and mechanical properties of porous advanced ceramics with XCT, demonstrating various features of the microstructure, including pore size, morphological analysis, micro-anisotropy, and spatial distribution of pores. Li *et al.*<sup>20</sup> analyzed the microstructure of SiO<sub>2f</sub>/SiO<sub>2</sub> composites by means of XCT, employing permeability and pore network models to study the impregnation process of silica sol. The aforementioned studies validate the superiority of XCT technology in characterizing the evolution of material structures and provide new insights into investigating the oxidation resistance processes of SiC<sub>f</sub>/SiC composites.

This study focuses on SiC<sub>f</sub>/SiC composites prepared using the commonly employed CVI+PIP combined process. The microstructure of the composites before and after exposure to high-temperature aqueous vapor was scanned and observed by means of XCT technology. On the basis of multi-scale qualitative and quantitative analyses of structural features such as porosity, matrix, and fibers, the oxidation process and mechanisms of SiC<sub>f</sub>/SiC composites in high-temperature aqueous vapor were investigated. The research presented in this paper provides direct theoretical and experimental references for the structural design and optimization of the oxidation resistance of SiC<sub>f</sub>/SiC composites.

## II. Materials and Methods

### (1) SiC<sub>f</sub>/SiC composite preparation

The SiC<sub>f</sub>/SiC composites utilized KD-II SiC fiber preforms as the reinforcement, woven in a 2.5D configuration. After the removal of the binder, a CVI process was employed to deposit SiC interfaces on the surface of the woven fibers. The CVI SiC matrix used methyltrichlorosilane (MTS) as a precursor, which was introduced into the reaction furnace via bubbling with H<sub>2</sub>, while argon (Ar) was used as a diluent gas. The total pressure within the furnace was maintained at 1.4 kPa, and the reaction temperature was controlled at 1075 °C. After deposition to a density of approximately 2.0 g/cm<sup>3</sup>, the PIP process was applied to further densify the composite materials by intro-

ducing SiC into the matrix. In the PIP process, polycarbosilane (PCS) was the precursor. The preforms were fully impregnated with PCS for 10–24 hours, with the initial cycle requiring 24 hours, with a curing temperature of 150 °C and a pyrolysis temperature of 1200 °C. A total of 10 PIP cycles was performed. The procedure of immersion-crosslinking-curing-pyrolysis was repeated until the weight gain was less than 1 %, ultimately yielding SiC<sub>f</sub>/SiC composites with a density of 2.5 g/cm<sup>3</sup>.

### (2) High-temperature aqueous-oxygen oxidation experiment

The high-temperature aqueous-oxygen oxidation experiment setup for the SiC<sub>f</sub>/SiC composite material was illustrated in the referenced literature<sup>21</sup>. The sample was placed in an alumina crucible to ensure sufficient contact with the gas flow. The oxidation temperature was set at 1300 °C, with a heating rate of 10 K/min during the first half and reduced to 5 K/min during the latter half. The steam generation device was activated when the specified temperature was reached, controlling the oxygen flow rate at 20 mL/min and the aqueous vapor flow rate at 50 mL/min. Insulation cotton was used to insulate the connecting pipe outside the furnace. The total oxidation duration was 160 hours.

### (3) XCT and data processing

XCT scanning tests were conducted in Sanying Precision Instruments Co., Ltd., with a nanoVoxel-2000 scanning system. When the sample installed on the rotating stage between the X-ray source and the detector rotates one complete turn, a set of images is recorded. This set of images is used to reconstruct a 3D image, where different grayscale values reflect the phase composition within the sample; regions with higher atomic numbers display greater grayscale values and appear brighter. In this study, to observe the microstructure of the samples before and after oxidation, two scanning resolutions were employed: one at 2.30 μm, which captures nearly the entire sample, and another at 0.94 μm, designed for observing more minor structural features. The test results were processed and analyzed using image processing software such as ImageJ, which aids in the analysis of the high-temperature aqueous-oxygen evolution process and oxidation mechanisms of the composite materials.

## III. Results and Discussion

### (1) Microstructural analysis of composites before oxidation

The structural schematic diagram of the 2.5D woven preform used in this study is shown in Fig. 1a. The weaving method employed is an orthogonal interlock weave between layers. This approach integrates several layers of weft fiber bundles arranged parallel to each other using warp fiber bundles in the thickness direction. Each warp fiber bundle interlocks only with the adjacent two layers of weft fiber bundles, and it passes through the adjacent rows of weft fiber bundles along the thickness direction. Hence, it is referred to as the orthogonal interlock weave

between layers<sup>22</sup>. It can be observed that the fibers in the woven preform are continuous in the warp and weft directions but discontinuous in the thickness direction, resulting in a structure with a distinct periodic pattern; thus, the volume fraction of fibers in different regions varies. The fibers at the intersection of the undulating warp fiber bundles and the straight weft fiber bundles exhibit a higher volume fraction, leading to a denser pore structure. In comparison, areas with unidirectional fiber bundles have a lower fiber volume fraction and a more porous structure.

The 3D model reconstructed from the data of the initial samples processed by XCT technology is shown in Fig. 1b. Since the fibers and the matrix are composed of SiC, the overall structure exhibits similar contrast levels. However, the wavy warp fiber bundles and straight weft fiber bundles can still be observed in the image. The 3D model of the extracted fibers (Fig. 1c) further illustrates the structural differences in fiber arrangement; the warp fibers are arranged layer by layer in the XZ plane, while the weft fibers are positioned only on the sides, resulting in a smaller fiber volume fraction in the center. The outer surface of the YZ plane is located at the intersection of the two types of fiber bundles, where the volume fraction is more significant. The overall extracted fiber volume fraction is 42.2%.

To further clarify the structural characteristics of SiC<sub>f</sub>/SiC composites prepared with the CVI+PIP combined process, typical 2D slices were selected from three different directions for microstructural analysis. First, out of 662 XY slices along the Z direction, five slices were sequentially selected: slices 1, 274, 333, 371, and 662, as shown in Fig. 2a-e. It can be observed that in the extracted XY plane, the warp SiC fiber bundles exhibit an elliptical cross-section. The weft fiber bundles, being approximately horizontal in the Z direction (Fig. 1b), provide an approximately rectangular cross-section along the length direction of the fiber bundles. The positions of these five slices along the Z direction differ, displaying the misalignment characteristics of the warp fiber bundles in the Y direction. For instance, in Fig. 2c and 2d, the warp fiber bundles are relatively well-aligned in the X and Y directions, while those in Fig. 2a, 2b, and 2e show poorer alignment. This misalignment of the warp fiber bundles further affects the pore structure. In aligned conditions, the pores in the XY plane are primarily arranged along the Y direction, resembling “inter-layer” pores of the warp

fiber bundles, as indicated in Fig. 2c. In contrast, “inter-layer” pores become staggered in misaligned situations, forming communicating pores, such as pore c marked in Fig. 2b. Looking at the XCT slice in Fig. 2f with higher magnification, the pores in the SiC<sub>f</sub>/SiC composites produced by the CVI+PIP combined process can still be classified into two common types: inter-bundle pores and intra-bundle pores. Inter-bundle pores are highlighted in the region marked in Fig. 2c; these pores are smaller when the matrix is more filled, as seen in pore a marked in Fig. 2a. Conversely, the original inter-fiber gap regions are retained mainly when the matrix filling is lower, as indicated by pore b marked in Fig. 2a. Intra-bundle pores, as shown in Fig. 2f, are longer along the fiber bundle direction, with smaller dimensions perpendicular to the fiber direction, typically below 100 μm. Overall, during the preparation process, the CVI matrix mainly fills the fiber bundle regions, as evidenced by the bright circular layers surrounding individual fibers visible in part f of the figure. Ultimately, the areas around the fiber bundles become relatively dense, with increasing intra-bundle pores towards the center. The PIP matrix fills the inter-bundle spaces, presenting a typical fragmented appearance. Due to the lower density of amorphous SiC, the contrast of the PIP matrix appears darker, allowing it to be distinguished more clearly in the images.

594 YZ slices were obtained in the X direction, and Figs. 3a-e display five characteristic slices: 1, 100, 300, 490, and 594. In contrast to the structures in the XY plane, the warp fiber bundles appear more flattened and exhibit a more orderly arrangement in each slice. The weft fiber bundles extend along the length direction, distributed in the interlayers of the warp fibers. The sequence of the five figures shows an overall reduction of the weft fibers from bottom to top (Figs. 3a and 3b), complete removal at Fig. 3c, followed by a filling process from bottom to top, ultimately returning to the high density shown in Fig. 3e. During the reduction or increase of the weft fibers, the composite structure displays distinct porous and less porous regions separated vertically (Figs. 3b and d). Since the weft fibers are located between the warp fibers, the pores serve as substitutes for their reduction, resulting in an overall layered distribution surrounding the warp fibers, predominantly along the Y direction, where larger pore sizes can exceed a millimeter, such as pore c in Fig. 3d.

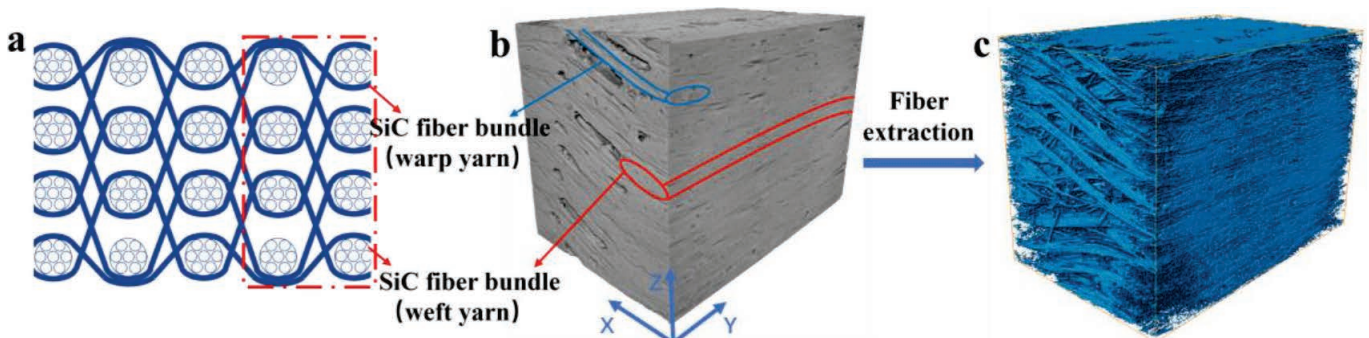


Fig. 1: (a) Schematic of the 2.5D-woven preform; (b) 3D reconstruction of SiC<sub>f</sub>/SiC composite; (c) 3D reconstruction of the extracted SiC fiber preform.

These inter-bundle pores are partially interrupted after matrix filling, as indicated in Fig. 3c, effectively reducing the length of the pores in the Y direction. The inter-layer pores also tend to extend across layers in the Z direction due to the irregular arrangement of the fiber bundles, as shown by pore a in Fig. 3b and pore b in Fig. 3c. Figs. 3a and e represent the outermost slices of the scanned overall structure, characterized by high density, with only a few small pores distributed in the narrow spaces between the bundles. An enlarged view in Fig. 3f further illustrates the internal structure of the fiber bundles, primarily showcasing the morphology of the intra-bundle pores and the fragmented appearance of the PIP matrix. Additionally, small microcracks generated by thermal stress were observed within the fiber bundles.

A total of 926 XZ slices was obtained in the Y direction, and five sectional images were selected in order: slices 74, 210, 365, 506, and 637, as shown in Fig. 4a-e. The material structure features exhibited in the XZ plane differ significantly from those in the previously discussed planes. This difference is primarily reflected in the wavy extension of the warp fiber bundles, which causes the inter-bundle pores to exhibit a similar directional distribution. The sequence from Fig. 4a to 4e presents the evolution of the warp fibers: crossing fibers – increasing from low to high – crossing fibers – decreasing from high to low – crossing fibers. With the weft fibers on both sides of the figure's cross-section, the higher fiber volume fraction results in denser regions on either side, with the inter-bundle pores predominantly distributed in the central

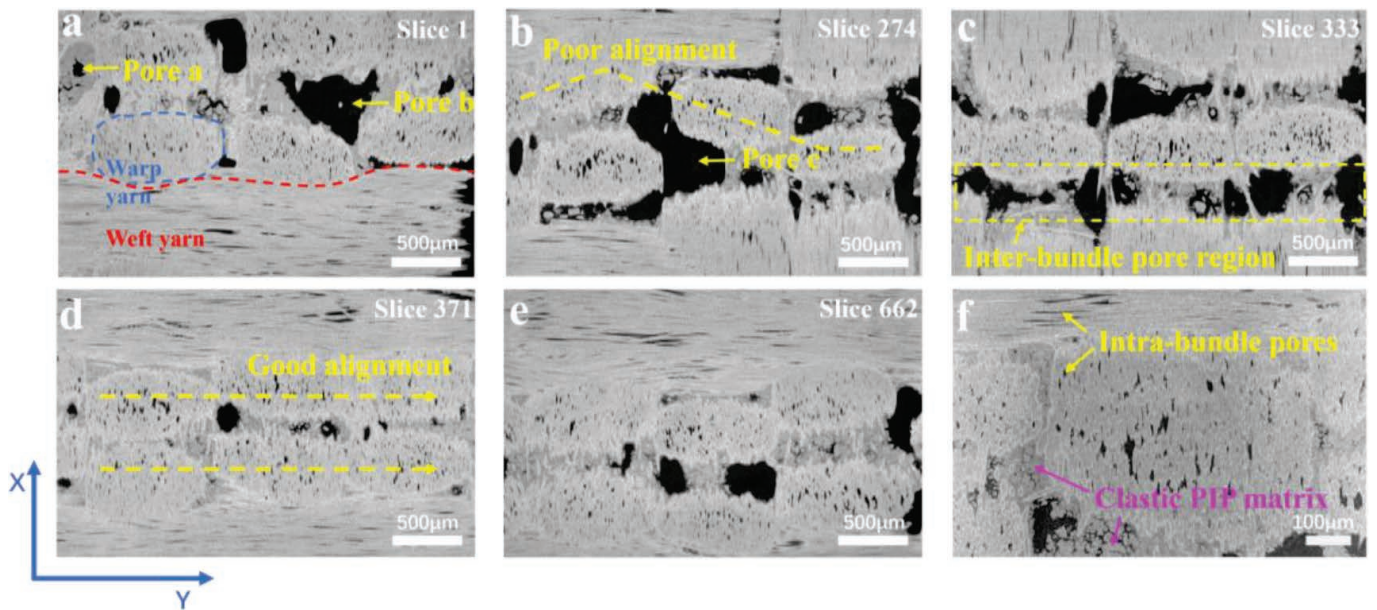


Fig. 2: 2D XCT images of 2.5D-woven SiC<sub>f</sub>/SiC specimen corresponding to different slice numbers in XY plane: (a)-(e) 2.30 μm resolution; (f) 0.94 μm resolution.

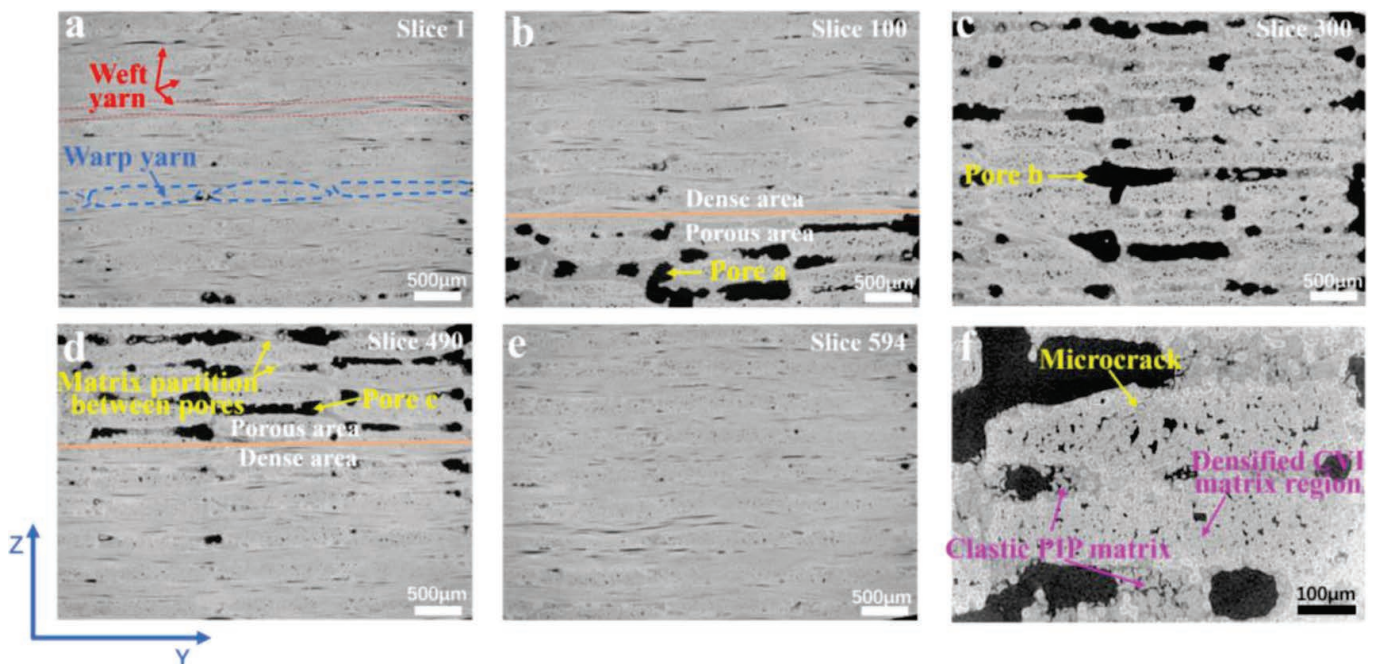


Fig. 3: 2D XCT images of 2.5D-woven SiC<sub>f</sub>/SiC specimen corresponding to different slice numbers in YZ plane: (a)-(e) 2.30 μm resolution; (f) 0.94 μm resolution.

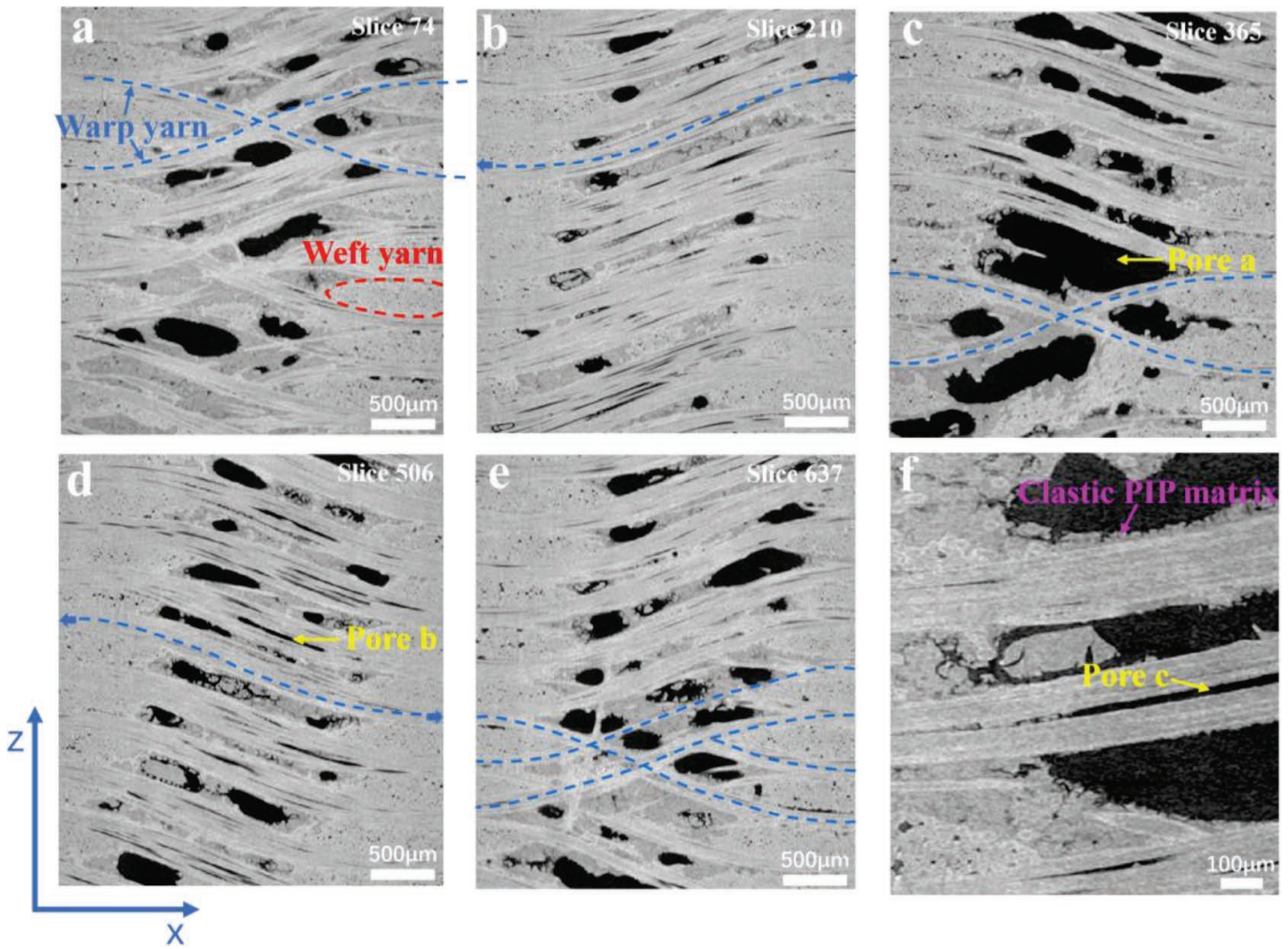


Fig. 4: 2D XCT images of 2.5D-woven SiC<sub>f</sub>/SiC specimen corresponding to different slice numbers in XZ plane: (a)-(e) 2.30 μm resolution; (f) 0.94 μm resolution.

area. Compared to the relatively consistent arrangement of the inter-bundle pores shown in Figs. 4b and 4d, there is a greater degree of fiber crossing in Figs. 4a and 4e, leading to the nearby pores being subdivided into smaller sections by the crossing fibers and the filling matrix. The wavy arrangement reduces the tightness of the warp fibers, making it easier for relatively larger intra-bundle pores to form, such as pore b in Fig. 4d and pore c in Fig. 4f. Additionally, larger inter-bundle pores can occur in the crossing areas of the warp fiber bundles due to reasons such as disordered arrangement or absence of fiber bundles, as shown by pore a in Fig. 4c. Fig. 4f provides a high-resolution magnified view of the XZ plane, clearly illustrating the structural characteristics of the PIP SiC matrix, which is primarily distributed around the fiber bundles.

Based on the observation of 2D slices, the pores of the composite material before oxidation were extracted, 3D-rendered, and quantitatively analyzed, with results shown in Fig. 5. Fig. 5a illustrates the 3D structure of all pores, which account for 10.9 % of the total volume of the sample, with an average pore volume of 525.14 μm<sup>3</sup>. Fig. 5b presents 3D models of large pores (those with a volume above the average) and small pores (those below the average). The former constitutes 95.8 % of the total pore volume, while the latter accounts for 4.2 %. Fig. 5c de-

picts the 3D extraction of through-pores that penetrate the sample and closed pores located within the sample. The through-pores are mainly formed by the interconnected inter-bundle pores displayed in Figs. 2–4, spanning all three directions of the sample. These represent the largest pores, reaching a volume of  $2.2 \times 10^7 \mu\text{m}^3$ , which comprises 55.26 % of the total pore volume and serves as a primary component of the overall porosity of the sample. The closed pores are primarily the intra-bundle pores indicated in Figs. 2–4. Furthermore, Fig. 5d provides a statistical analysis of the number, total volume, and proportion of pores across different orders of magnitude based on pore volume. The statistical method involves summarizing and sorting the number and volume dimensions of pores extracted after threshold segmentation, categorizing them into different magnitude levels. It is evident that although the number of tiny pores is exceptionally high, their total volume and proportion are the lowest. In contrast, the higher-order large pores categorized as  $10^5$ ,  $10^7$ , and  $10^8$  consist of only 9, 3, and 1 instance, respectively (representing the largest inter-bundle openings mentioned earlier), yet these large pores occupy a substantial portion of the volume and pore ratio. This observation is consistent with the previous analysis of pore structures in the slices.

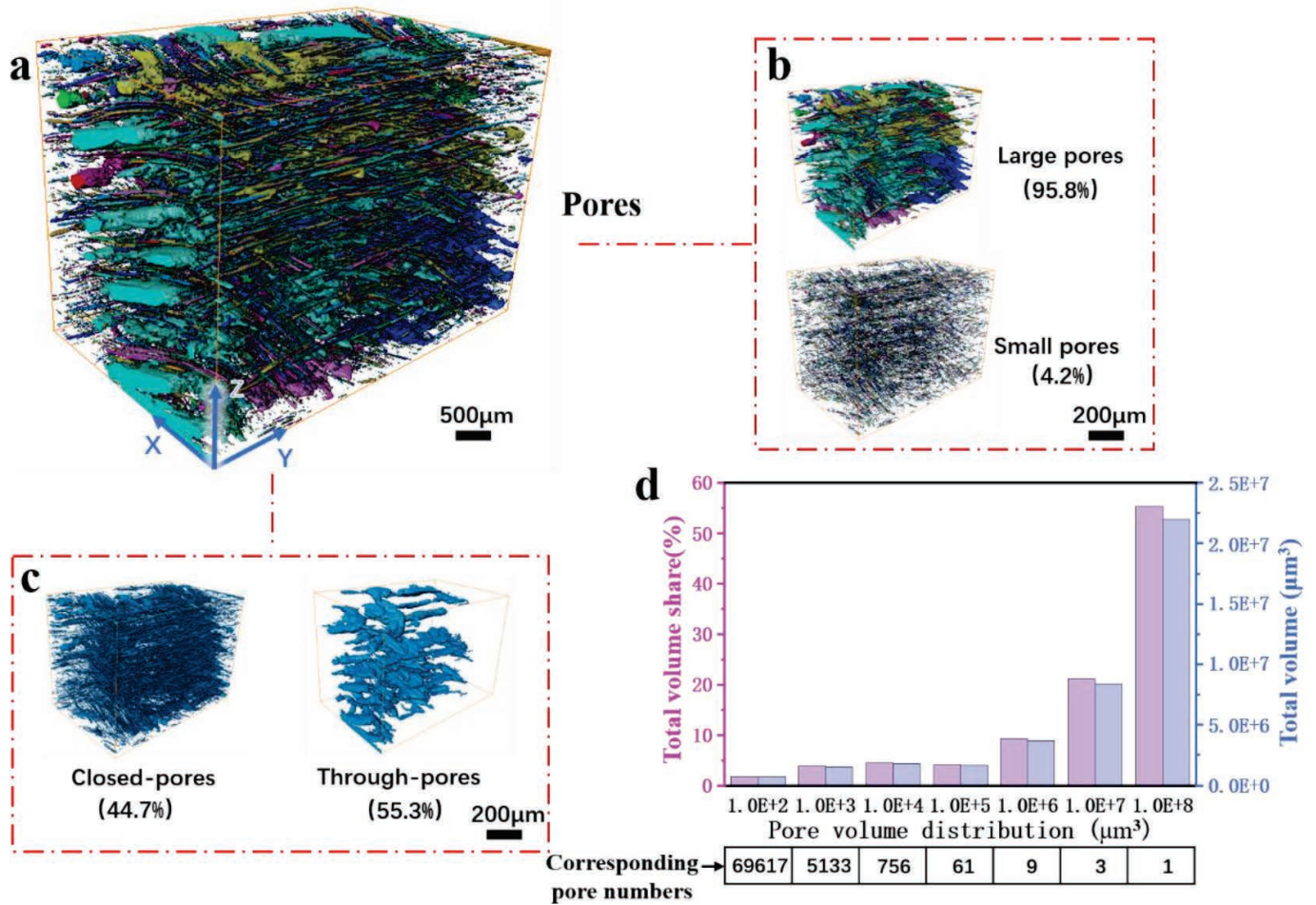


Fig. 5: Pore analysis: (a) 3D Extraction of pores; (b) 3D Extraction of large and small pores; (c) 3D Extraction of closed and through pores; (d) Statistics on the number and volume share of pores.

## (2) Microstructural analysis of composites after oxidation

To investigate the microstructural damage of  $\text{SiC}_f/\text{SiC}$  composites under high-temperature aqueous-oxygen conditions, a comparative analysis was conducted of the XCT data obtained before and after oxidation. Fig. 6 presents the area fraction curves of pores across three directions, layer by layer, before and after oxidation. To demonstrate the reduction in pore size, the slices corresponding to the maximum difference between the pre- and post-oxidation curves were selected and displayed in Fig. 7. Fig. 6 shows that the pores in all three directions significantly decreased after oxidation, indicating a reduction in the overall porosity of the sample. In the XY plane comparison shown in Fig. 6a, the pore distribution before and after oxidation exhibits periodic oscillations, primarily due to the inherent periodic distribution of fibers in the Z direction. The most considerable difference in pore area fraction is located at slice 640. A comparison of the slice images in Fig. 7a and 7b reveals that the PIP matrix at the edge of the fiber bundles generated a substantial amount of oxidized material after oxidation, filling the inter-bundle pores and significantly reducing pore volume. In the YZ plane curve shown in Fig. 6b, the maximum difference in pore area fraction occurred at slice 240, with most of the pore volume reduction

occurring in the central region. This is attributed to the higher fiber volume fraction and density at both ends of the composite, resulting in fewer pores. At the same time, the central region has more pores in comparison, allowing for easier filling by the oxidized materials after oxidation. Observing the slice comparisons in Fig. 7c and 7d, the filling of oxidized material and the reduction in pore volume are also very pronounced, especially in the edge regions of the YZ plane. The decrease in pores in the XZ plane is more uniform, as seen in Fig. 6c, with the maximum difference at slice 370. It can be observed from the slices before and after oxidation that the large area of the SiC matrix between the fiber layers was oxidized, forming a continuous oxidative pathway through the left and right sides of the sample.

Fig. 8 presents high-resolution enlarged slice images extracted before and after oxidation to illustrate the detailed oxidation phenomena. In Figs. 8a and 8c, initial microcracks have expanded severely after oxidation, with oxidized materials filling these cracks, and some cracks even penetrating through entire fiber bundles (Fig. 8b). The matrix cracks observed in Fig. 8c became exacerbated after oxidation, transforming into the oxidized channels depicted in Fig. 8d. From the post-oxidation slices, it can be observed that only a small portion of the CVI matrix within the bundles has undergone oxidation, indicating that the

SiC matrix in the bundles is less susceptible to oxidation. In Fig. 8e, the relatively regular-shaped PIP SiC matrix in the large pores was unable to fully fill the pores after oxidation

tion, resulting in an irregular appearance. It is evident that the PIP SiC matrix is more prone to significant oxidation compared to the CVI matrix.

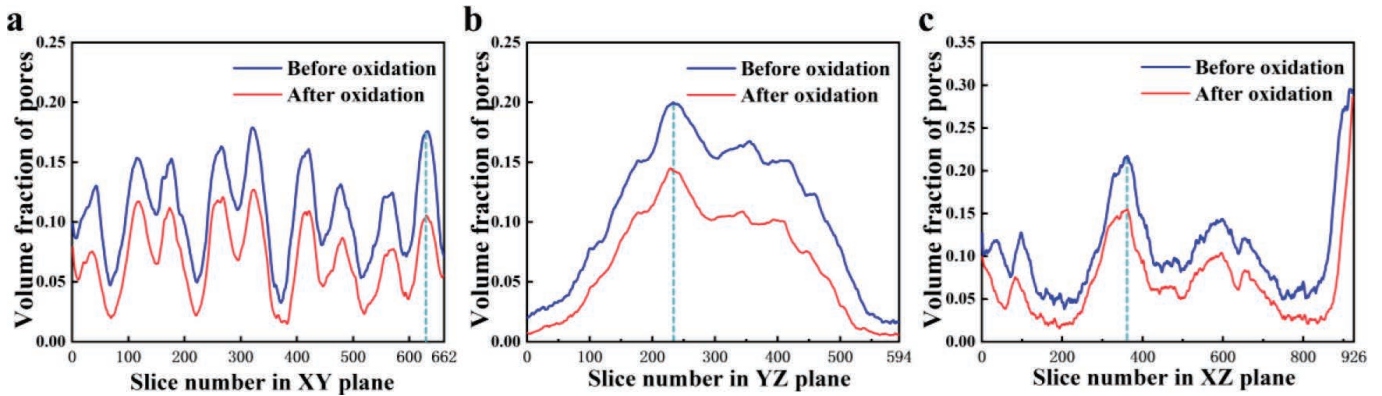


Fig. 6: Layer-by-layer area ratio of pores along three directions, before and after oxidation: (a) XY slices; (b) YZ slices; (c) XZ slices.

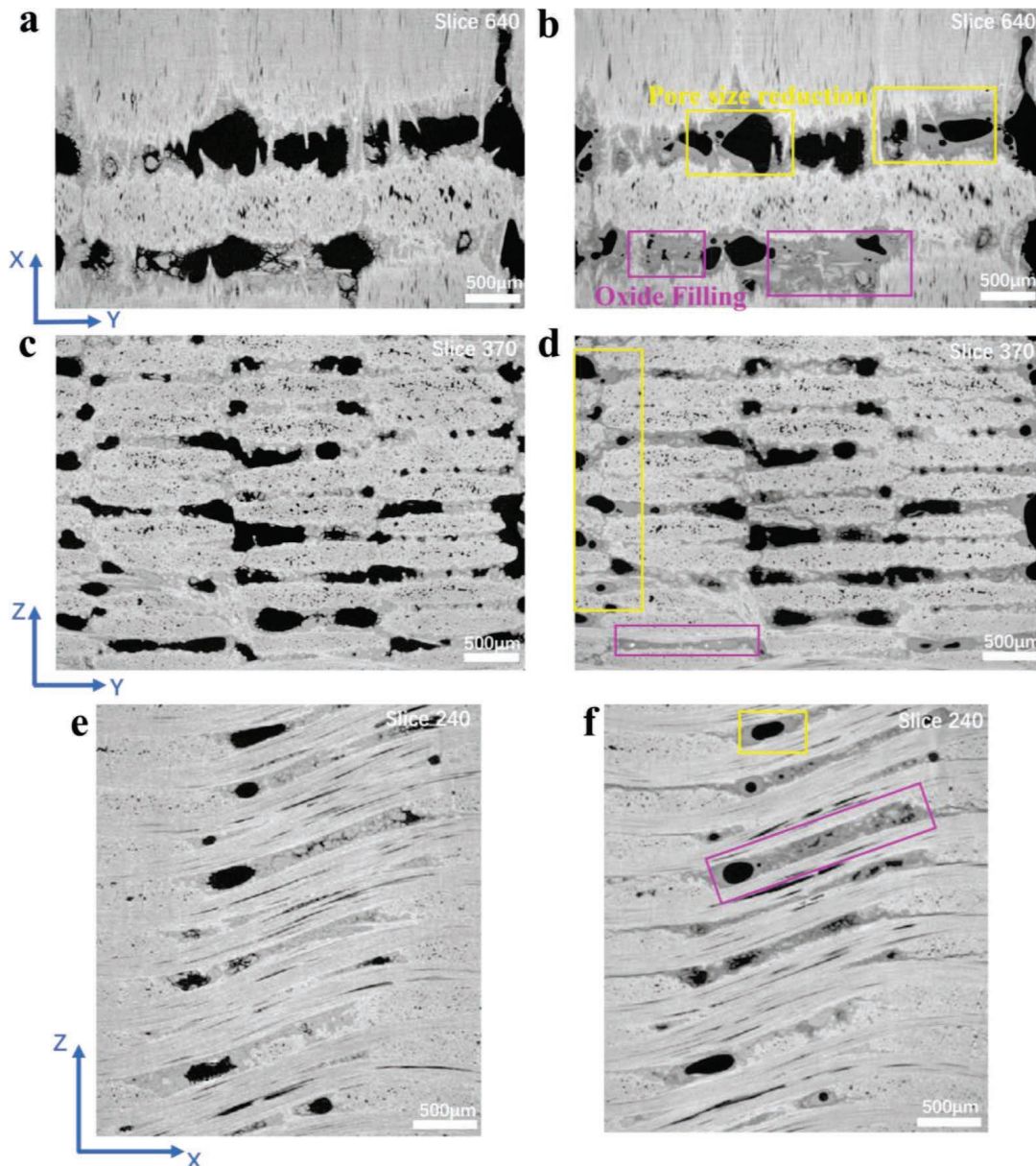
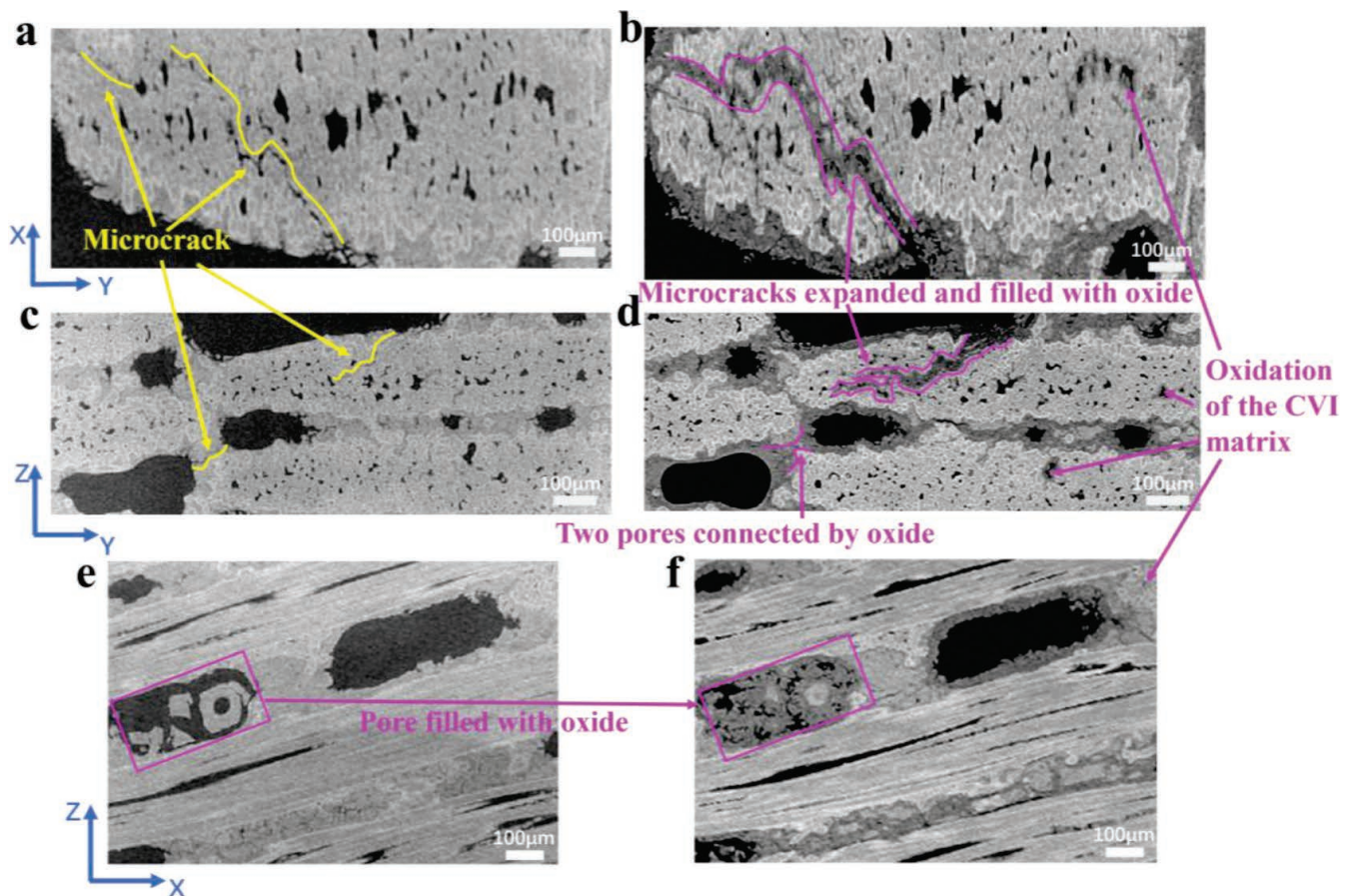


Fig. 7: Comparison of slices before and after oxidation at the maximum difference point of the layer-by-layer area ratio of pores along three directions: (a-b) XY slices; (c-d) YZ slices; (e-f) XZ slices.



**Fig. 8:** High-resolution images showing microstructures before and after oxidation in three directions: (a) XY slice before oxidation; (b) XY slice after oxidation; (c) YZ slice before oxidation; (d) YZ slice after oxidation; (e) XZ slice before oxidation; (f) XZ slice after oxidation.

To further elucidate the oxidation process of the CVI matrix described above, enlarged images from the YZ plane in the thickness direction (Figs. 9a-d) and the XZ plane in the length direction (Figs. 9e-h) were selected for analysis within the fiber bundles. As shown in Fig. 9a, oxidized materials enter the bundle through small channels opened by loosely arranged single fibers at the edges of the fiber bundles. Figs. 9b-d illustrate the subsequent oxidation process of the matrix along the pores within the bundle. Fig. 9e depicts an oxidation channel generated by a fracture defect at the edge of the fiber bundle. In contrast, Figs. 9f-h demonstrate the continued oxidation extension into the bundle's internal pores. It is evident that once oxygen penetrates the interstitial pores of the bundle, these pores act as carriers for oxygen, leading to the oxidation of the surrounding CVI matrix. However, the influx of oxygen is not continuous; oxidized materials within the bundle can block the entry points for additional oxygen. In closed interstitial pores, once the small amount of oxygen that has entered is fully consumed, the oxidation process within the bundle ceases. Consequently, the extent of oxidation is limited to the vicinity of the interstitial pores and does not propagate further into other areas of the CVI matrix. Furthermore, due to the limitations imposed by XCT resolution and its inability to provide elemental distribution information, there is minimal observation of oxidation occurring in the CVI matrix under normal conditions within the fiber bundles.

The 3D reconstruction of all pore models after oxidation is shown in Fig. 10a. The total volume of all pores accounts for 6.8 % of the sample volume, representing a significant reduction in pore proportion compared to the initial sample before oxidation. The average volume of the pores after oxidation is  $626.6 \mu\text{m}^3$ . Fig. 10b displays large pores above the average volume and tiny pores below the average volume, comprising 96.0 % and 4.0 % of the total pore volume, respectively, which is not significantly different from the initial sample. However, no results were obtained when data was extracted on the through-pores after oxidation. This indicates that the most enormous inter-bundle openings in the initial sample were subdivided into smaller pores after oxidation. The pores were extracted after oxidation based on threshold segmentation, and their quantity and volume size were summarized, sorted, and statistically analyzed. Fig. 10c illustrates the proportion of different magnitudes of pores before and after oxidation, clearly demonstrating this phenomenon. There are no large pores in the order of  $10^8 \mu\text{m}^3$  after oxidation. Correspondingly,  $10^7 \mu\text{m}^3$  pores increased from 21.15 % to 65.96 %, while  $10^6 \mu\text{m}^3$  pores rose from 9.34 % to 17.66 %. This suggests that the substantial filling of oxidized materials post-oxidation has effectively blocked various pore channels, leading to the differentiation of larger pores into smaller ones. The pore channels serve as pathways for oxidation by oxygen and aqueous vapor, and the blockage caused by the oxidized materials can effectively inhibit further oxidation processes.

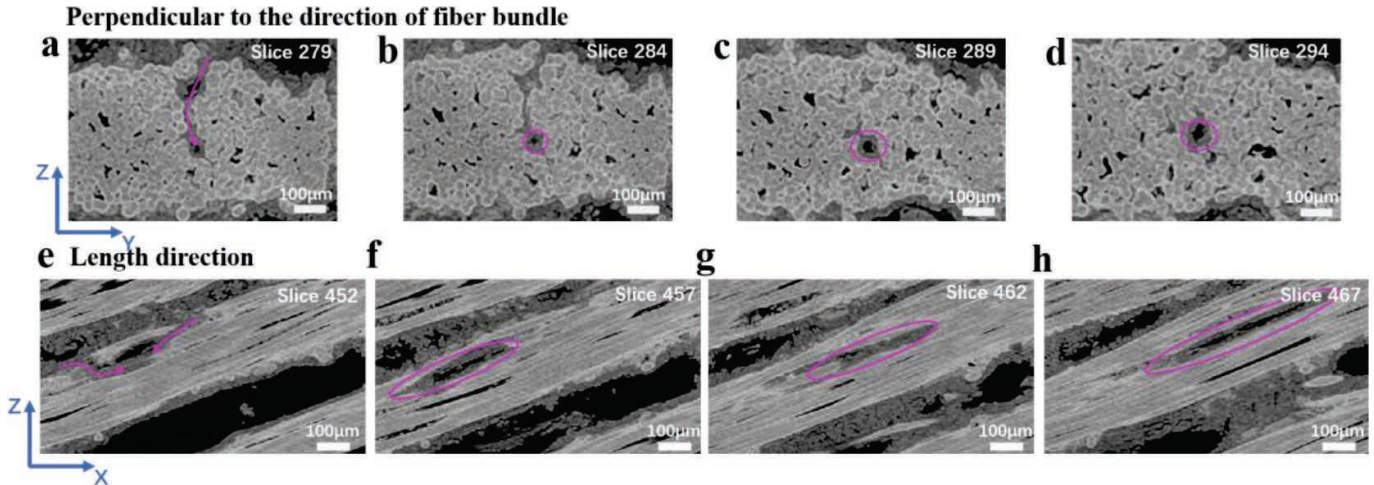


Fig. 9: Oxidation process of the CVI matrix: (a-d) Thickness direction of YZ slice; (e-h) Length direction of XZ slice.

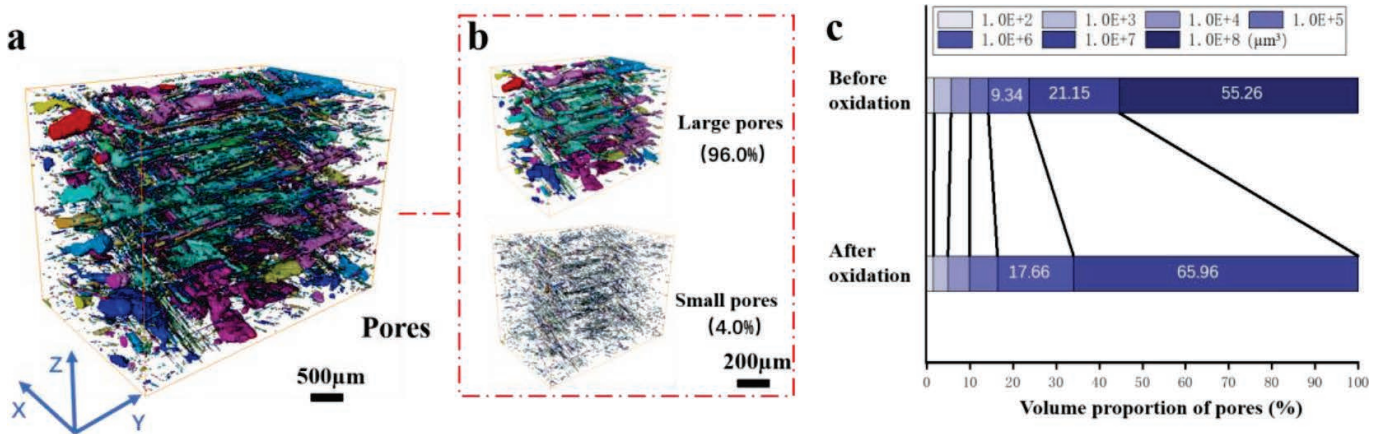


Fig. 10: Extraction and distribution of 3D models of pores after oxidation: (a) All pores; (b) Large and small pores; (c) Pore volume distribution before and after oxidation.

Fig. 11a presents the extracted skeleton model of large pores before oxidation, where the pore channels run through the sample, providing unobstructed pathways for oxygen. Fig. 11b shows the skeleton model of large pores after oxidation, significantly reducing overall volume, particularly at the sides. The central pores have contracted less, as the edge pores have shrunk in volume due to oxidation, and some have been blocked by oxidized materials, making it difficult for oxygen to reach the center for further oxidation. Three characteristic pore models are identified from the skeleton of the large pores after oxidation. Fig. 11c illustrates an edge pore where two pores connect into one as they shrink in volume after oxidation, indicating that the oxidized materials exhibit flowability. Fig. 11d depicts a large pore in the center, while Fig. 11e shows a communicating pore connected to the edge pore. In Figs. 11c and 11e, many bubble-like pores can be distinctly observed attached to the periphery of the large pores, with smooth edges and narrower channels, contrasting sharply with the irregular pores before oxidation. This characteristic diminishes until it disappears as it extends into the central pore, where Fig. 11d retains the original features of the pore, showing a chaotic structure at the edges. Although the central region in Fig. 11e is con-

nected to the edge region, the characteristics of the pores in the center align with those in Fig. 11d. Despite oxygen reaching the center of the sample along the pore channels, the oxidation conditions at the center differ from those at the edge positions. This indicates that during the erosion process of high-temperature aqueous-oxygen oxidation, the extent of corrosion in the outer region is significantly greater than that in the inner region.

Fig. 12 illustrates the layered area ratio curves of the matrix (including oxidized materials after oxidation) before and after oxidation in three directions. Fig. 13 compares slices at the intersection points of the curves before and after oxidation. Since there are still unoxidized matrix regions in the samples post-oxidation, the matrix and oxide were extracted from the oxidized samples to facilitate comparison. From the three sets of curves in Fig. 12, it is evident that the overall curve initially decreases and then increases, which aligns with the structural analysis of the initial sample discussed earlier. The increase in oxidized materials post-oxidation does not alter this trend. However, the curves for the central region in all three directions show a more pronounced increase after oxidation, leading to the emergence of intersection points between the pre- and post-oxidation curves.

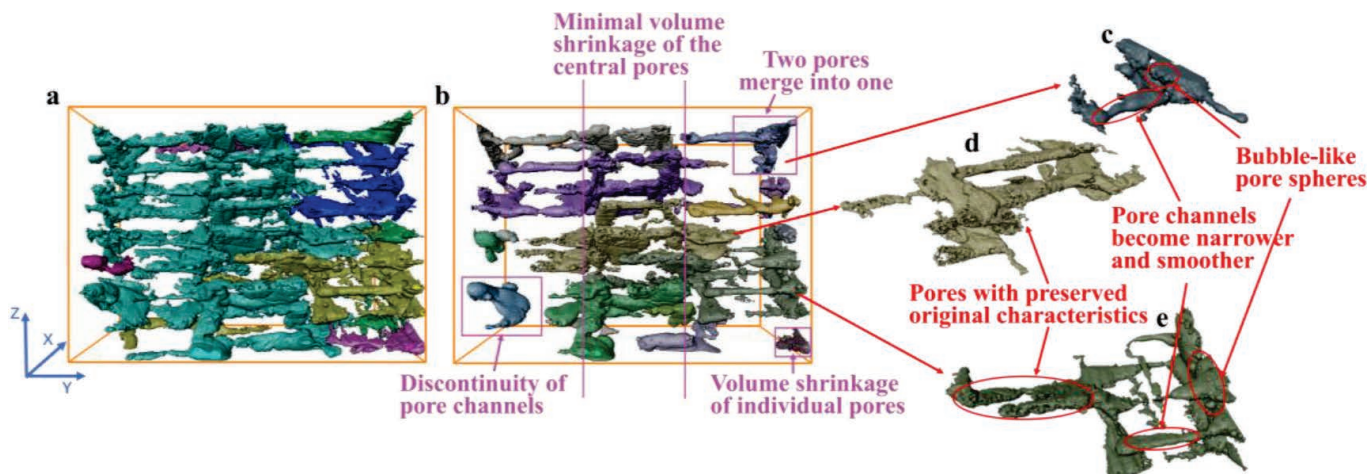


Fig. 11: 3D model of the macropores framework (a) before and (b) after oxidation, and single pore extracted from the oxidized model: (c) Pore at the edge position; (d) Pore at the central position; (e) Pore connecting the edge and central position.

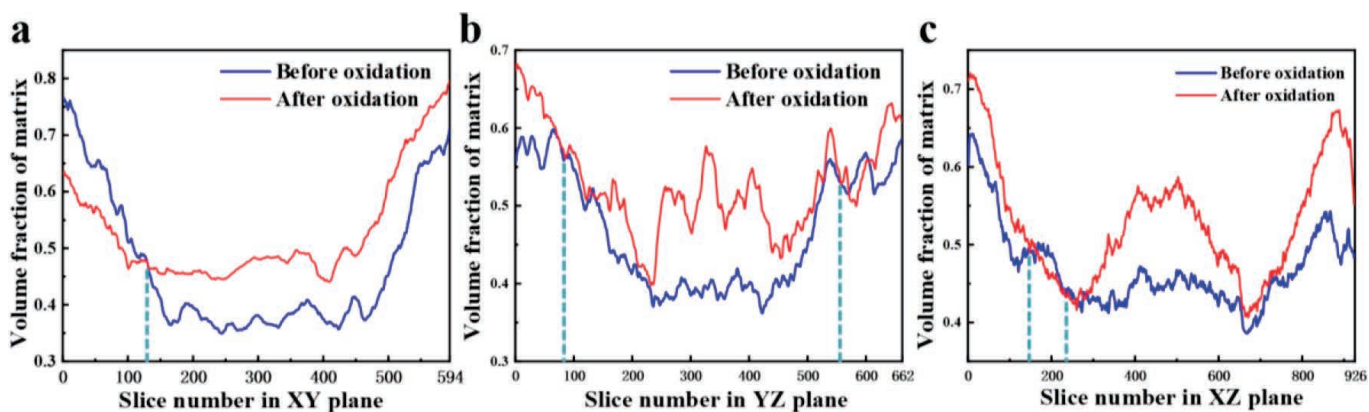


Fig. 12: Layer-by-layer area ratio of the matrix along three directions before and after oxidation: (a) XY slices; (b) YZ slices; (c) XZ slices.

In contrast, the volume of pores after oxidation is consistently lower than that of the initial sample, indicating that SiC fibers are eroded by high-temperature aqueous oxygen during oxidation. The oxidation primarily occurs at the edges of the fiber bundles, making it challenging to penetrate the interior of the bundles. Only in the case of cracks serving as pathways for oxygen, as shown in Fig. 13d, does oxidation occur within the fiber bundles. The oxidative erosion at the edges has led to a significant loss of peripheral and terminal fibers, evidenced by a noticeable reduction in fiber length along the longitudinal direction (Fig. 13b). Additionally, the thickness of the elliptical fiber bundles has decreased (Fig. 13d), and some individual fibers have experienced minor displacement or even fracture (Fig. 13f). The partial oxidative degradation of SiC fibers under high-temperature aqueous and oxygen conditions suggests that the oxidation process is exceedingly aggressive.

Fig. 14a presents a 3D model of the enormous skeleton of the oxidized materials after oxidation, showcasing an overall layered stacking structure. This is more clearly observed in the left view (Fig. 14b) and the front view (Fig. 14c). From the left view, the outer oxidized materi-

al on the far left exhibits a layer structure that progresses from high to low (as depicted from front to back in Fig. 14c). Similarly, the outer oxidized material on the far right also displays this trend. In contrast, the central region shows a reverse layering structure, progressing from high to low (from back to front in the frontal view). This overall structural arrangement of the oxidized materials aligns with the previously described fiber structure, and the position of the blue lines in the figure is basically determined by the direction of the fiber bundles shown in Figs. 3–4, belonging to the inter-bundle regions. As proved in Fig. 5, the connectivity of the inter-bundle pores is high, so it is easy for oxygen to enter the channel. Corrosion damage accordingly developed from the surrounding area of the inter-bundle pores into the fiber bundle. The PIP matrix in the inter-bundle region has higher oxidation degree after oxidation, which helped to form a connected sheet-like and layered oxide structure, as shown in Fig. 15. The 3D display of the oxide skeleton intuitively reflects the regional distribution of oxidation damage within the tested composite, and also provides a certain reference for the analysis of oxidation pathways.

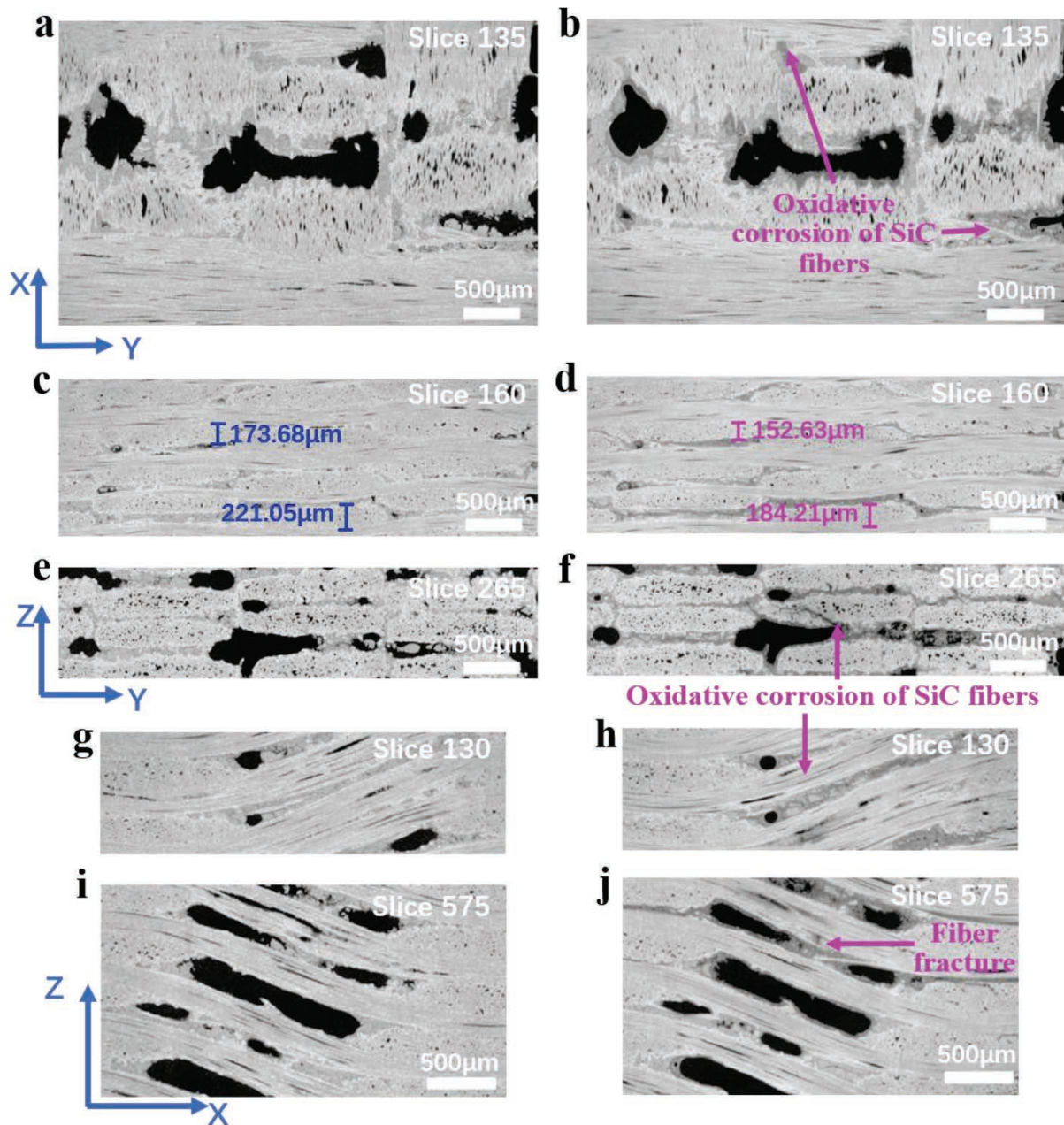


Fig. 13: Comparison of slices before and after oxidation at the maximum difference point of the layer-by-layer area ratio of pores along three directions: (a-c) XY slices; (d-f) YZ slices; (g-i) XZ slices.

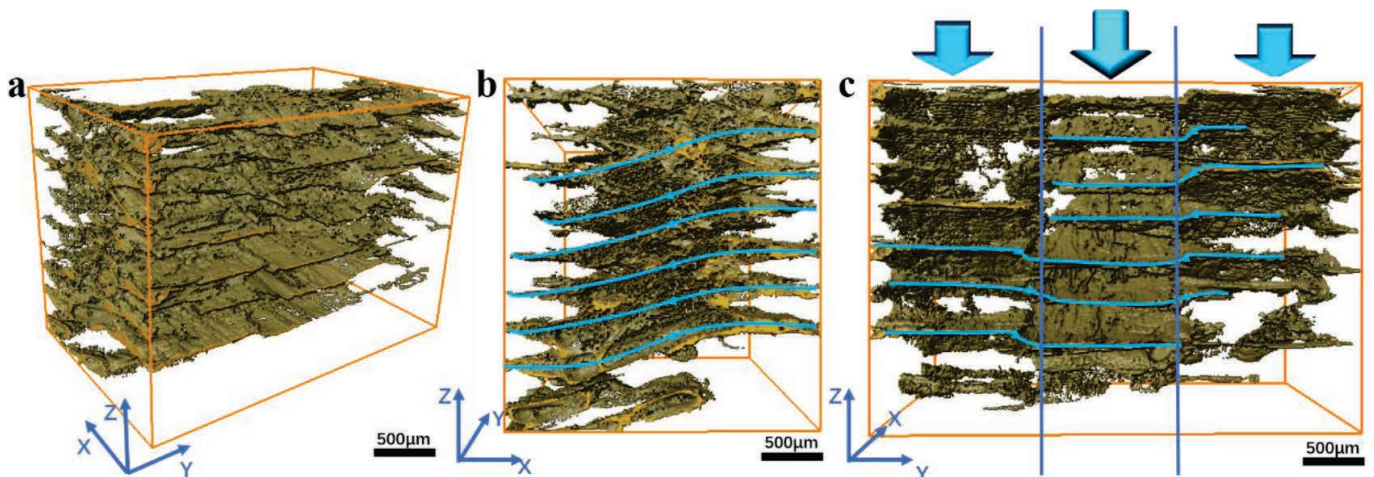


Fig. 14: Sketch illustration of the oxide skeleton after oxidation of SiC<sub>f</sub>/SiC composites: (a) 3D model, (b) Left view, and (c) Front view.

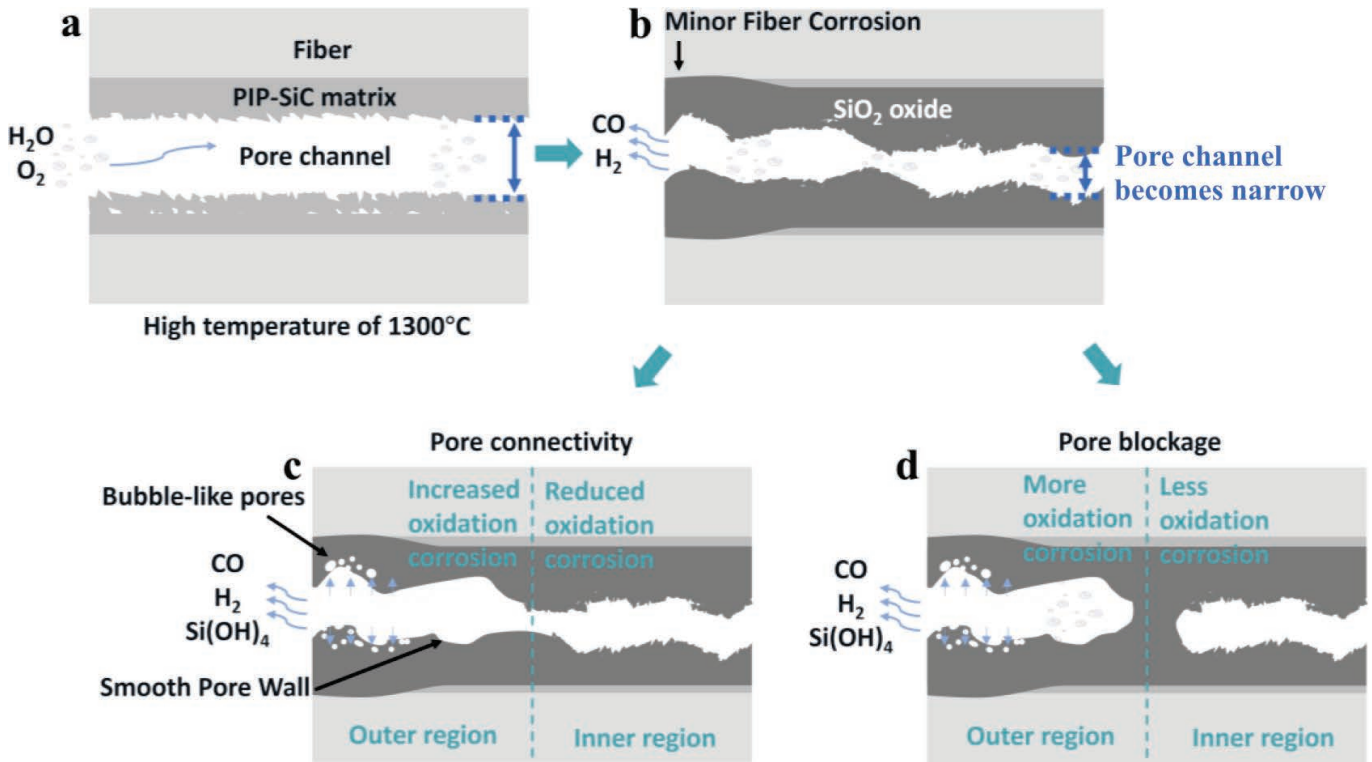
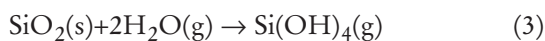
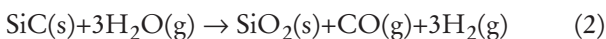
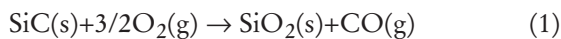


Fig. 15: The oxidation mechanism diagram of composite materials in high-temperature aqueous and oxygen.

### (3) Oxidation mechanism

Based on the images and data extracted from XCT, a comparative analysis of the samples before and after oxidation allows for precise observation of the oxidation damage to SiC<sub>f</sub>/SiC composites under high-temperature aqueous-oxygen coupling conditions. This includes the location and morphological characteristics of fibers, pores, matrix, and oxides, providing an adequate basis for analyzing the oxidation mechanisms of SiC<sub>f</sub>/SiC composites in high-temperature aqueous-oxygen environments. According to the literature, the main reaction mechanisms of SiC in high-temperature aqueous-oxygen conditions are as follows<sup>23,24,25</sup>:



In a high-temperature aqueous-oxygen coupling environment, the aqueous-oxygen corrosive medium reacts with SiC to form a protective SiO<sub>2</sub> oxidation layer. The SiO<sub>2</sub> further reacts with aqueous vapor to produce volatile Si(OH)<sub>4</sub>, which is carried away by the airflow. Due to the continuous and dense nature of the CVI-prepared SiC matrix<sup>26</sup>, it effectively protects the fibers from erosion by aqueous oxygen, exhibiting good resistance to aqueous-oxygen corrosion<sup>27</sup>. Consequently, as mentioned earlier, only a minimal amount of the CVI matrix and SiC fibers are oxidized. In contrast, the PIP SiC matrix is situated in large inter-bundle pores. It contains small internal voids, which serve as channels for aqueous-oxygen penetration, making the inter-bundle PIP SiC highly susceptible to oxidative corrosion. This observation is consistent with the

previously discussed oxidation analysis of the SiC matrices produced by the two methods.

By integrating the oxidation reaction mechanisms of SiC<sub>f</sub>/SiC composites with the analysis of the sample properties before and after oxidation presented above, we can summarize the oxidative evolution process of SiC<sub>f</sub>/SiC composites in high-temperature aqueous-oxygen environments. As illustrated in the oxidation mechanism diagram (Fig. 15), aqueous-oxygen penetrates the interior of the samples through external pores, with the large pore skeleton serving as the primary channel. Under the erosive action of aqueous-oxygen, the PIP SiC matrix quickly undergoes passive oxidation to form SiO<sub>2</sub>, as indicated by Reaction (1). At high temperatures, this SiO<sub>2</sub> exists in a molten state<sup>28</sup> and possesses some degree of fluidity, which facilitates the formation of a dense oxidation layer. Portions of this layer can even block the pores. Furthermore, SiO<sub>2</sub> has a low oxygen diffusion coefficient<sup>29</sup>, which impedes further oxidative erosion of the sample's internal structure. According to Reaction (3), the oxidation layer of SiO<sub>2</sub> continues to react with aqueous vapor to produce volatile Si(OH)<sub>4</sub>, leading to the ongoing consumption of the protective oxidation layer. Moreover, the action of H<sub>2</sub>O can damage the network structure of SiO<sub>2</sub>, leading to a more severe degree of erosion. From these three reactions, it is evident that when aqueous is involved in the oxidation reactions, both the SiC matrix and the SiO<sub>2</sub> protective layer are consumed simultaneously, accompanied by the release of substantial amounts of gas (CO, H<sub>2</sub>, Si(OH)<sub>4</sub>). Consequently, the oxidative corrosion in high-temperature aqueous-oxygen environments is vigorous.

Based on the summarized oxidation process, the structural evolution of pores with different morphological features described in Fig. 11 can be explored. During the oxidation process, aqueous oxygen penetrated into the sample through the external edge pores, and many of the channels were rapidly blocked by the SiO<sub>2</sub> generated from oxidation (Fig. 11). Consequently, aqueous oxygen became more concentrated in the outer regions, where SiO<sub>2</sub> was further consumed by water vapor. A large amount of gas produced from the reaction (primarily Si(OH)<sub>4</sub>) also accumulated within the outer pore channels, with some escaping through the external pores, while a portion penetrated further into the surroundings along the molten SiO<sub>2</sub>, forming spherical pores of varying sizes around the oxidized material. At the same time, the incoming aqueous oxygen repeatedly washes the molten SiO<sub>2</sub> on the pore walls with the escaping gases, causing the oxidized material to fill the channels and narrow them, while the gas flow smooths and levels the pore walls. Therefore, the extent of oxidized material consumption in the external region is greater than that in the internal region, a feature that can be clearly observed in the oxidized skeleton shown in Fig. 14C. XCT effectively captures the 3D structures of the pore channels, spherical bubble-like pores, and oxidized skeleton, providing a more intuitive and clear perspective to assist in analyzing the high-temperature aqueous-oxygen oxidation process of the composite material.

#### IV. Conclusions

This study employs synchrotron X-ray computed tomography (XCT) to establish a three-dimensional degradation atlas of SiC<sub>f</sub>/SiC composites fabricated via chemical vapor infiltration (CVI) and polymer infiltration pyrolysis (PIP) hybrid processing during high-temperature aqueous-oxygen corrosion. The XCT-derived microstructure quantification reveals a dual-scale porosity architecture: CVI-derived matrix preferentially infiltrates intra-tow regions, leaving intra-bundle pores with low tortuosity, while PIP-processed matrix deposits at inter-bundle zones, forming interconnected pore channels dictated by the 2.5D fiber architecture. Comparative analysis of pre/post-corrosion tomography datasets demonstrates that oxidation initiates through gas-phase oxygen penetration along inter-bundle pore networks, evidenced by channel diameter reduction and surface roughness decrease. The concomitant formation of vesicular porosity at specimen peripheries correlates with volatile species evolution during SiC matrix oxidation. These findings provide mechanistic insights into the spatially heterogeneous corrosion behavior through a novel 3D damage quantification paradigm. The methodology establishes a non-destructive evaluation framework for optimizing matrix architecture in SiC<sub>f</sub>/SiC composites, particularly for aerospace thermal protection systems requiring graded oxidation resistance. Future work should integrate *in situ* XCT with thermogravimetric-differential scanning calorimetry (TG-DSC) to resolve transient oxidation dynamics.

#### Acknowledgments

The authors gratefully acknowledge the financial support of the Hunan Provincial Natural Science Foundation (2023JJ40671), National Natural Science Foundation of China (No. 52202123) and National University of Defense Technology Project (KY0405072423).

#### References

- 1 Luo, H., Chen, B., Huang, H.: Development strategy of continuous silicon-carbide-Fiber-reinforced silicon carbide ceramic matrix composites in the field of advanced nuclear energy, *Strateg. Study CAE*, **26**, 53 (2024).
- 2 Park, J.Y.: SiCf/SiC composites as core materials for Generation IV nuclear reactors. *Structural Materials for Generation IV Nuclear Reactors*, 441–470, (2017).
- 3 Zhao, G., Jiang, Z., Xi, H.: Ultrahigh-temperature mechanical behavior and failure mechanisms of SiCf/SiC composites, *Ceram. Int.*, **49**, 39391–39399, (2023).
- 4 Wu, S., Chen, J., Zhang, X.: Recent advances in interphase engineering for improved behavior of SiCf/SiC composites, *J. Eur. Ceram. Soc.*, **44**, 6797–6814, (2024).
- 5 Wang, P., Liu, F., Wang, H.: A review of third generation SiC fibers and SiCf/SiC composites. *J. Mater. Sci. Technol.*, **35**, 2743–2750, (2019).
- 6 Hu, J., Liu, C., Ye, F.: A review on high-performance SiCf/SiC composites prepared by PIP process, *J. Mater. Res. Technol.*, **33**, 7216–7235, (2024).
- 7 Han, T., Luo, R., Cui, G.: Effect of SiC nanowires on the high-temperature microwave absorption properties of SiCf/SiC composites, *J. Eur. Ceram. Soc.*, **39**, 1743–1756, (2019).
- 8 De Meyere, R.M.G., Gale, L., Harris, S.: Optimizing the fiber push-out method to evaluate interfacial failure in SiC/BN/SiC ceramic matrix composites, *J. Am. Ceram. Soc.*, **104**, 2741–2752, (2021).
- 9 Quan, H., Wang, L., Huang, J.: Durable protection and failure mechanism of the multilayer coating system for SiCf/SiC composites under high-temperature oxidation, *Compos. Part B Eng.*, **244**, 110197, (2022).
- 10 Du, J., Liu, R., Wan, F.: Failure mechanism of ytterbium silicate/silicon bi-layer environmental barrier coatings on SiCf/SiC composites upon long-time water vapor and oxygen corrosion test, *Surf. Coat. Technol.*, **447**, 128871, (2022).
- 11 Mainzer, B., Jemmali, R., Watermeyer, P.: Development of damage-tolerant ceramic matrix composites (SiC/SiC) using Si-BN/SiC/pyC fiber coatings and LSI processing, *J. Ceram. Sci. Tech.*, **8**, 113–120, (2017)
- 12 Wang, P., Wang, Q., Zhang, X.: Oxidation behavior of SiCf/SiC composites modified by Layered-Y<sub>2</sub>Si<sub>2</sub>O<sub>7</sub> in wet oxygen environment, *J. Inorg. Mater.*, **34**, 904, (2019).
- 13 Wang, L., Luo, R., Cui, G.: Oxidation resistance of SiCf/SiC composites with a PyC/SiC multilayer interface at 500 °C to 1 100 °C, *Corros. Sci.*, **167**, 108522, (2020).
- 14 Ji, S., Liang, B., Hu, C.: Mechanical properties and oxidation behaviors of self-healing SiCf/SiC-SiBCN composites exposed to H<sub>2</sub>O/O<sub>2</sub>/Na<sub>2</sub>SO<sub>4</sub> environments, *Acta Metall. Sin. Engl. Lett.*, **36**, 1909–1923, (2023).
- 15 Li, J., Liu, Y., He, F.: Preparation and properties of SiC/SiC-SiYC with excellent water-oxygen corrosion resistance, *J. Eur. Ceram. Soc.*, **43**, 6606–6611, (2023).
- 16 Wang, L., Yuan, K., Luan, X.: 3D characterizations of pores and damages in C/SiC composites by using X-ray computed tomography, *Appl. Compos. Mater.*, **26**, 493–505, (2019).
- 17 Puchakayla, P.K.R., Pegu, B., Gandhi, P.: Defects evolution during printing, debinding and sintering for additive manufacturing of yttria stabilized zirconia, *Mater. Charact.*, **221**, 114752, (2025).

- 18 Niu, G., Sano, T., Hogan, J.D.: Internal damage evolution investigation of C/SiC composites using in-situ tensile X-ray computed tomography testing and digital volume correlation at 1000 °C, *Compos. Part Appl. Sci. Manuf.* **163**, 107247, (2022).
- 19 Lo, C., Sano, T., Hogan, J.D.: Microstructural and mechanical characterization of variability in porous advanced ceramics using X-ray computed tomography and digital image correlation, *Mater. Charact.*, **158**, 109929, (2019).
- 20 Li, C., Wang, Y., Liu, R.: Microstructure analysis of quartz fiber reinforced SiO<sub>2</sub> matrix composites by X-ray computed tomography, *Mater. Charact.*, **209**, 113745, (2024).
- 21 Jian, Y., Wang, Y., Liu, R.: Property evolutions of Si/mixed Yb<sub>2</sub>Si<sub>2</sub>O<sub>7</sub> and Yb<sub>2</sub>SiO<sub>5</sub> environmental barrier coatings completely wrapping up SiCf/SiC composites under 1300 °C water vapor corrosion, *Ceram. Int.*, **47**, 22373–22381, (2021).
- 22 Younes, R., Zaki, W.: Optimal weaving for 2.5D interlocks, *Compos. Struct.*, **93**, 1255–1264, (2011).
- 23 Opila, E.J.: Variation of the oxidation rate of silicon carbide with water-vapor pressure, *J. Am. Ceram. Soc.*, **82**, 625–636, (1999).
- 24 Terrani, K.A., Jung, Y.I., Kim, H.G.: Silicon carbide oxidation in steam up to 2 MPa, *J. Am. Ceram. Soc.*, **97**, 2331–2352, (2014).
- 25 Park, D.J., Jung, Y.I., Kim, H.G.: Oxidation behavior of silicon carbide at 1200 °C in both air and water-vapor-rich environments, *Corros. Sci.*, **88**, 416–422, (2014).
- 26 Hao, J., Li, J., Shi, W.: Antioxidant coating composed of SiC on carbon fibers by chemical vapor reaction, *J. Ceram. Sci. Technol.*, **9**, 465–470, (2018).
- 27 Bhatt, R.T., Jaskowiak, M.H.: Creep and cyclic durability of CVI SiC/SiC composites. *J. Eur. Ceram. Soc.*, **44**, 4437–4451, (2024).
- 28 Gao, J., Deng, D., Luo, X.: Ablation and molten layer flow simulation for plate model of SiO<sub>2</sub>f/SiO<sub>2</sub> composite material using particle method, *Comput. Fluids*, **284**, 106436, (2024).
- 29 Honda, M., Yamasaki, Y., Tanoue, K.: Dependence of oxygen concentration and temperature on the growth rate distribution of SiO<sub>2</sub> solid film by chemical vapor deposition in the Hexamethyldisiloxane-oxygen system, *J. Jpn. Inst. Energy*, **100**, 186–193, (2021).